



Cite this: *Chem. Commun.*, 2023,
59, 13715

Received 28th July 2023,
Accepted 25th October 2023

DOI: 10.1039/d3cc03658h

rsc.li/chemcomm

Intra-cluster energy transfer editing in a dual-emitting system to tap into lifetime thermometry†

Claudia Manuela Santos Calado, Diogo Alves Gálico and Muralee Murugesu *

The impact of composition control and energy transfer on luminescence thermometry was investigated in a Tb^{III}/Eu^{III} dual-emitting molecular cluster-aggregate, known as {Ln₂₀}. The study of lifetime dynamics sheds new light on how one can take advantage of rational planning to enhance thermometric performance and gaining insights into intriguing optical properties.

Over the past decade, luminescence thermometry has emerged as a valuable tool for advancing remote temperature sensing. With its remarkable spatial resolution (<10 μm), high relative thermal sensitivity (>1% K⁻¹) and rapid acquisition times, its potential applications span from biomedicine to photonics and nanoelectronics.¹ This technique relies on the correlation between temperature and the luminescence properties of a material, including the intensity and spectral position of emission bands, as well as the lifetime (τ) of emitting states. By analysing this thermally dependent signal, a thermometric parameter (Δ) is obtained, and its performance can be assessed using the thermal relative sensitivity (S_R), as expressed in eqn (1).²

$$S_R (\%) = \left| \left(\frac{\delta \Delta}{\delta T} \right) \cdot \frac{1}{\Delta} \right| \times 100 \quad (1)$$

Lanthanide (Ln^{III})-doped materials are highly sought after in luminescence thermometry due to the distinctive optical features of 4f elements.^{3,4} The 4f–4f electronic transitions give rise to unique emission profiles with narrow bands, displaying characteristic energy positions and long lifetimes, making them reliable thermometric parameters.¹ In addition, the control of luminescent processes through chemical composition and the use of established models to understand thermally induced spectral variations offer significant advantages for practical applications.^{5–7} Among the various platforms available for designing Ln^{III}-based luminescent thermometers, molecular cluster-aggregates (MCAs) are

particularly distinguished for their tuneable architectures and outstanding luminescent performances.⁸ Owing to their crystalline nature, MCAs possess a rigid metal core with high-nuclearity, precise coordination environment, and uniformity within a single unit. They also allow control over energy transfer (ET) processes and their influence on optical output *via* composition control. We have previously reported a highly tuneable icosanuclear MCA with the general formula [Ln₂₀(chp)₃₀(CO₃)₁₂(NO₃)₆(H₂O)₆]·H₂O, {Ln₂₀}, where chp = deprotonated 6-chloro-2-pyridinol (Fig. 1a and Fig. S1, ESI†). Through composition and ET modulation, we demonstrated fine-tuning of optical properties, including downshifting and upconversion luminescence, adjustment of colour output, and their impact on promising applications such as optical barcoding and luminescence intensity ratio thermometry.^{7,9,10}

With these studies in mind, herein we report a series of {Ln₂₀} MCAs, namely {Eu₁Tb₁₉} (1), {Eu₂Tb₁₈} (2), {Eu₃Tb₁₇} (3) and {Eu₄Tb₁₆} (4), and investigate these molecular materials as τ-based luminescent thermometers. By carefully varying the amount of Eu^{III} and Tb^{III} in the composition, we achieve precise control over intra-cluster ET processes. Our main focus is to understand how these processes impact the temperature-dependent luminescence behaviour. Specifically, we aim to provide control over the decay of Eu^{III} and Tb^{III} emitting states to enhance the potential of our MCAs as τ-based luminescent thermometers. Using τ as a thermometric parameter offers significant advantages for data acquisition and treatment, including insensitivity to fluctuations in excitation power, light scattering, and reflections.^{1,11} To improve the S_R performance, we explore a ratiometric approach based on the ratio between Eu^{III} ⁵D₀ and Tb^{III} ⁵D₄ τ (τ_{Eu} and τ_{Tb}, respectively). Our dual-emitting centre MCA, with two optically active ions in the metal core, helps develop a rational understanding of τ-based thermometry and thermal sensitivity in a molecular system. Our focus is on optimizing these features by considering variations in composition and data treatment.

We prepared MCAs 1, 2, 3 and 4 according to the previously reported procedure (Table S1, ESI†).⁹ Powder X-ray diffractograms (PXRD) confirm that the compounds are isostructural to

Department of Chemistry and Biomolecular Sciences, University of Ottawa, 10 Marie Curie, Ottawa, Ontario, K1N 6N5, Canada. E-mail: m.murugesu@uottawa.ca
† Electronic supplementary information (ESI) available. See DOI: <https://doi.org/10.1039/d3cc03658h>



Fig. 1 (a) Molecular core of {Ln₂₀} MCAs. Structure shown refers to {Eu₄Tb₁₆}. Ln^{III} are randomly assigned. Color code: green for Tb^{III}, salmon for Eu^{III} and red for oxygen. (b) Partial energy level diagram of {Ln₂₀} MCAs. ISC = intersystem crossing; ET = energy transfer; LMCT = ligand-to-metal charge transfer. (c) Emission decay curves of Eu^{III} 5D₀ (700 nm) and Tb^{III} 5D₄ (545 nm) of {Eu₁Tb₁₉}, obtained at -5 °C (cold) and 60 °C (hot), λ_{exc} = 300 nm.

the icosanuclear {Ln₂₀}, which crystallizes in the $R\bar{3}$ space group (Fig. S2, ESI†). Fourier transform infrared (FTIR) spectra show the expected molecular vibrations (Fig. S3, ESI†), while energy-dispersive X-ray spectroscopy (EDS) data qualitatively confirm the presence of Ln^{III} ions in each MCA (Fig. S4, ESI†). ICP-OES supports the nominal chemical composition, with a good agreement between theoretical and experimental Ln^{III} ratio. Photoluminescent studies were carried out in acetonitrile (0.1 mg mL⁻¹), as the stability of the {Ln₂₀} MCA in this solvent has been demonstrated by NMR spectroscopy in previous works.¹² Further experimental details are available in the ESI.†

To enhance the absorption coefficient of Ln^{III} ions, molecular systems often utilize organic ligands as “antennas” to absorb photons. Subsequently, the ligands transfer the absorbed energy to the Ln^{III} emitting centre, populating its 4f excited states. In the {Ln₂₀} MCA, the chp ligand plays the role of a sensitizing antenna, with triplet state (T₁) energy reported at 24 961 cm⁻¹. From that level, the luminescent processes expected for the Eu^{III}/Tb^{III} pair are well-known (Fig. 1b).⁹ Due to the favourable position of Tb^{III} 5D₄ excited state (≈ 20 500 cm⁻¹) relative to chp T₁, an efficient T₁ → Tb^{III} ET takes place, resulting in emission bands within the visible range characteristic of Tb^{III}. However, direct sensitization of Eu^{III} 5D₀ excited state (≈ 17 500 cm⁻¹) by chp T₁ is not efficient, leading to non-radiative deactivation through an Eu-based ligand-to-metal charge transfer (LMCT) state at 20 492 cm⁻¹.¹² The characteristic Eu^{III} emission bands are only observed due to an efficient Tb^{III} → Eu^{III} ET, which leads to the population of Eu^{III} 5D₀. Thus, Tb^{III} acts as a bridging pathway that allows the electronic population to reach Eu^{III} emitting state.

By changing the Tb^{III}/Eu^{III} composition in our MCAs series, we can assess the influence of Tb^{III} → Eu^{III} ET and the efficiency of this process, along with side non-radiative deactivation pathways (such as the LMCT state), on the population of both Tb^{III} 5D₄ and Eu^{III} 5D₀ emitting states targeted for τ thermometry (Fig. 1c). The observed τ reflects the contribution of all radiative (emission of light) and non-radiative processes (vibration, energy transfer, charge-transfer state, etc.) leading to the deactivation of an emitting state. Therefore, accounting for these processes is critical for understanding the emission dynamics, τ behaviour with temperature, and the impact on thermometric performance.

The excitation and emission spectra of all MCAs were collected at 20 °C. The presence of an intense broad band centred at 300 nm, assigned to the chp excited singlet state (S₁), and the absence of noticeable 4f–4f transition bands indicate an efficient antenna effect (Fig. S5, ESI†). Under 300 nm excitation, MCAs exhibit characteristic sharp bands assigned to Tb^{III} (5D₄ → 7F_J, J = 6–0) and Eu^{III} (5D₀ → 7F_J, J = 0–4) electronic transitions (Fig. S6, ESI†). While **1** shows a higher intensity of Tb^{III} emission bands, the rest of the series displays a higher intensity of Eu^{III} components. This impacts the colour output of each MCA. MCA **1** displays a yellow-greenish output, while **4** exhibits an orange-reddish emission (Fig. S7, ESI†), which agrees with the change in Tb^{III}/Eu^{III} ion ratio in the composition. Emission decay curves of Tb^{III} 5D₄ and Eu^{III} 5D₀ emitting states collected at 20 °C (Fig. 2a and b) show a multiexponential decay profile due to the presence of four different crystallographic sites occupied by Ln^{III} ions within the {Ln₂₀} asymmetric unit. Average τ (⟨τ⟩) values were calculated from decay curves as expressed by eqn (2), where t₀ is the time at which the curve hits its maximum intensity (I), and t₁ is the time when it reaches the background.¹³

$$\langle \tau \rangle = \frac{\int_{t_0}^{t_1} t \cdot I(t) \cdot dt}{\int_{t_0}^{t_1} I(t) \cdot dt} \quad (2)$$

At a constant temperature (20 °C), the τ of both emitting centres shortens with an increase in Eu^{III} content. In either case, the radiative process accounted by the observed τ is the emission of light. Regarding τ_{Tb}, the Tb^{III} → Eu^{III} ET is the



Fig. 2 Emission decay curves of {Eu₁Tb₁₉} (**1**), {Eu₂Tb₁₈} (**2**), {Eu₃Tb₁₇} (**3**) and {Eu₄Tb₁₆} (**4**) MCAs monitoring (a) Tb^{III} 5D₄ (545 nm) and (b) Eu^{III} 5D₀ (700 nm) emitting states. Collected at 20 °C, λ_{exc} = 300 nm.

main non-radiative deactivation pathway present in all systems. Thus, a higher number of Eu^{III} ions in the MCA leads to a higher probability of ET, resulting in a faster depopulation of $^5\text{D}_4$. In the case of τ_{Eu} , besides the non-radiative contribution of the LMCT state, the higher number of Eu^{III} ions leads to concentration quenching and increases the likelihood of Eu^{III} occupying different crystallographic sites, which impacts the average τ .

To better understand these photophysical properties and assess the MCAs' potential as τ -based luminescent thermometers, we collected variable temperature emission decay curves of Tb^{III} $^5\text{D}_4$ and Eu^{III} $^5\text{D}_0$, ranging from -5°C to 60°C (Fig. S8 and S9, ESI†). As illustrated in Fig. 3a and b, τ_{Tb} increases with rising temperature, while τ_{Eu} decreases under the same conditions. The trend for Tb^{III} suggests that at higher temperatures excited vibrational levels coupled with the Tb^{III} $^5\text{D}_4$ have a higher probability of being occupied, as expected according to Boltzmann distribution, leading to a slower depopulation of this emitting state. Conversely, Eu^{III} $^5\text{D}_0$ becomes more easily deactivated at higher temperatures since it increases the probability of energy loss through non-radiative routes.

To gain a deeper understanding of these characteristics and assess the efficiency (η_{ET}) of $\text{Tb}^{\text{III}} \rightarrow \text{Eu}^{\text{III}}$ ET in each system, structurally analogous MCAs were prepared by replacing the emitting Eu^{III} ions with Gd^{III} . As the first excited 4f level of Gd^{III} ($^6\text{P}_{7/2}$, $32\,200\text{ cm}^{-1}$) is too high in energy relative to both chp T_1 and Tb^{III} $^5\text{D}_4$, it is an optically inactive ion in this system. Thus, we were able to compare the τ of the donor ion (Tb^{III}) in the presence (τ_{a}) and the absence (τ_0) of the acceptor ion (Eu^{III}) (Fig. S10 ESI†), and calculate η_{ET} using eqn (3).¹⁴

$$\eta_{\text{ET}} (\%) = \left[1 - \left(\frac{\tau_{\text{a}}}{\tau_0} \right) \right] \times 100 \quad (3)$$

As depicted in Fig. 3c, at a constant temperature (20°C), the increase of Eu^{III} content in the MCA results in the enhancement



Fig. 3 Average τ values of (a) Tb^{III} $^5\text{D}_4$ (545 nm) and (b) Eu^{III} $^5\text{D}_0$ (700 nm) emitting states of $\{\text{Eu}_1\text{Tb}_{19}\}$ (**1**) (green), $\{\text{Eu}_2\text{Tb}_{18}\}$ (**2**) (orange), $\{\text{Eu}_3\text{Tb}_{17}\}$ (**3**) (purple) and $\{\text{Eu}_4\text{Tb}_{16}\}$ (**4**) (pink) MCAs, as well as $\text{Tb}^{\text{III}} \rightarrow \text{Eu}^{\text{III}}$ ET efficiency (η) at (c) 20°C and (d) variable temperatures.

of η_{ET} , which corroborates $\text{Tb}^{\text{III}} \rightarrow \text{Eu}^{\text{III}}$ ET as the main pathway of non-radiative depopulation of Tb^{III} $^5\text{D}_4$. This leads to the population of Eu^{III} $^5\text{D}_0$ at the expense of Tb^{III} $^5\text{D}_4$. In general, the efficiency of ET processes is highly influenced by temperature, with significant effects typically observed at lower temperatures ($< 0^\circ\text{C}$).¹⁵ In our study, as the temperature increases, the efficiency decreases (Fig. 3d and Table S2, ESI†). This effect is more pronounced in **1**, where η_{ET} decreases from 44.2% to 39.4%, and less evident in **4**, where it changes from 94.0% to 93.4%. The varying behaviour is attributed to the more noticeable increase in τ_{Tb} with temperature in **1** compared to **4**.

Based on these results, we explored the tuning of intra-cluster $\text{Tb}^{\text{III}} \rightarrow \text{Eu}^{\text{III}}$ ET of our series of MCAs to investigate their potential as τ -based thermometers. More specifically, we decided to take advantage of the two τ with different tendencies in our systems to investigate their suitability for ratiometric thermometry. We chose as Δ the ratio between $\tau_{\text{Tb}}/\tau_{\text{Eu}}$, and also τ_{Eu} itself for comparison purposes, on the premise that the opposite trends of Tb^{III} and Eu^{III} , where τ_{Tb} increases and τ_{Eu} decreases according to temperature, would have a positive impact on sensitivity and favour a higher S_{R} .

The temperature dependence of Δ is shown in Fig. 4a and b. A logistic function (eqn (S1), ESI†) was used for the mathematical fitting of Δ values. It is valid to point out that this function has no physical meaning and was used just for fitting purposes. To evaluate the thermometric performance, S_{R} curves were obtained by applying the fitted function to eqn (1). Further details about thermometry data treatment, including thermal resolution (Fig. S11, ESI†), are available in the ESI.†

Using only τ_{Eu} as a Δ , we observe an enhancement of S_{R} according to the increase of Eu^{III} ions in the MCA composition. While **1** shows a maximum S_{R} (S_{Rmax}) value of $1.7\%^\circ\text{C}^{-1}$ at 60°C , at this same temperature, **4** displays an S_{Rmax} of

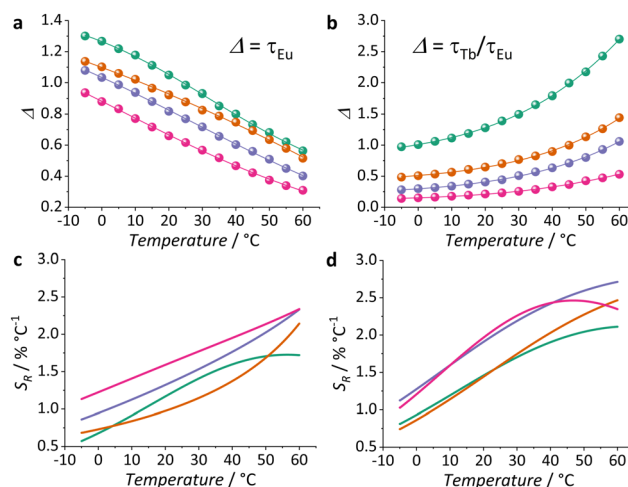


Fig. 4 Temperature dependence of (a) τ_{Eu} and (b) $\tau_{\text{Tb}}/\tau_{\text{Eu}}$ ratio as thermometric parameters (Δ) of MCAs $\{\text{Eu}_1\text{Tb}_{19}\}$ (**1**) (green), $\{\text{Eu}_2\text{Tb}_{18}\}$ (**2**) (orange), $\{\text{Eu}_3\text{Tb}_{17}\}$ (**3**) (purple) and $\{\text{Eu}_4\text{Tb}_{16}\}$ (**4**) (pink). Inserted lines show the mathematical fitting of logistic function. Relative thermal sensitivities (S_{R}) of (c) τ_{Eu} and (d) $\tau_{\text{Tb}}/\tau_{\text{Eu}}$ ratio are also given for the MCAs with the same color scheme.

2.3% °C⁻¹. This behaviour is somehow expected once the LMCT state quenching depends on the number of Eu^{III} present. Since this is the main non-radiative deactivation pathway of Eu^{III} ⁵D₀, it will govern the temperature dependence of τ_{Eu} . On top of that, the increase of η_{ET} seems to favor a higher S_{R} . However, a beneficial impact on thermometry is observed only to a certain extent, as **3** and **4** exhibit the same trend and S_{Rmax} values.

When we consider the $\tau_{\text{Tb}}/\tau_{\text{Eu}}$ ratiometric approach and compare it to τ_{Eu} data (single approach), an interesting improvement of S_{Rmax} is observed. While **1** displays S_{Rmax} of 2.1% °C⁻¹, **3** shows a value of 2.7% °C⁻¹, both at 60 °C. This represents an enhancement higher than 22% for **1** and 15% for **3** in comparison to the single approach. Within the ratiometric approach and considering the trend observed for the other MCAs, **4** shows a slight reduction in performance, with S_{Rmax} of 2.5% °C⁻¹ at 45 °C. In this case, in addition to the thermally-driven effect of LMCT on τ_{Eu} , we also have to consider the behaviour of τ_{Tb} itself. For all compositions, τ_{Tb} exhibits a considerable increase according to temperature. The highest increase is observed for **3** (37%), while **4** (22%) has the lowest. Therefore, the degree of τ_{Tb} temperature susceptibility greatly impacts the ratiometric approach outcome. While $\tau_{\text{Tb}}/\tau_{\text{Eu}}$ improves the thermometric performance, one must consider how much advantage can be practically derived from each specific system being explored.

The values of S_{Rmax} obtained in this study are comparable to those observed for other τ -based thermometers (Table S4, ESI[†]), ranging from nanoparticles to molecular compounds. Notably, our MCAs exhibit significantly better performance than other reported molecular systems. To the best of our knowledge, this is the first time τ has been employed as a thermometric parameter for a Ln^{III}-based MCA. This result highlights the unique advantages of MCAs as they strike a balance between nanoparticles and molecular systems, combining high nuclearity in a nanometric size with precise control over composition and coordination environment. We anticipate that the insights gained from this study will pave the

way for the development of other dual-centre systems with potential for τ -based thermometry.

This work was supported by the Canadian Foundation for Innovation, and the Natural Sciences and Engineering Research Council of Canada.

Conflicts of interest

There are no conflicts to declare.

Notes and references

- 1 C. D. S. Brites, S. Balabhadra and L. D. Carlos, *Adv. Opt. Mater.*, 2019, **7**, 1801239.
- 2 J. Zhou, B. Rosal, D. Jaque, S. Uchiyama, D. Jin, B. del Rosal, D. Jaque, S. Uchiyama and D. Jin, *Nat. Methods*, 2020, **17**, 967–980.
- 3 A. Skripka, A. Benayas, R. Marin, P. Canton, E. Hemmer and F. Vetrone, *Nanoscale*, 2017, **9**, 3079–3085.
- 4 D. M. Lyubov, A. N. Carneiro Neto, A. Fayoumi, K. A. Lyssenko, V. M. Korshunov, I. V. Taydakov, F. Salles, Y. Guari, J. Larionova, L. D. Carlos, J. Long and A. A. Trifonov, *J. Mater. Chem. C*, 2022, **10**, 7176–7188.
- 5 A. Ćirić and M. D. Dramićanin, *J. Lumin.*, 2022, **252**, 119413.
- 6 L. Li, X. Tang, Z. Wu, Y. Zheng, S. Jiang, X. Tang, G. Xiang and X. Zhou, *J. Alloys Compd.*, 2019, **780**, 266–275.
- 7 D. A. Gállico and M. Murugesu, *Angew. Chem., Int. Ed.*, 2022, **61**, e202204839.
- 8 D. A. Gállico, C. M. S. Calado and M. Murugesu, *Chem. Sci.*, 2023, **14**, 5827–5841.
- 9 D. A. Gállico, A. A. Kitos, J. S. Ovens, F. A. Sigoli and M. Murugesu, *Angew. Chem., Int. Ed.*, 2021, **60**, 6130–6136.
- 10 D. A. Gállico, R. Ramdani and M. Murugesu, *Nanoscale*, 2022, **14**, 9675–9680.
- 11 K. Elzbieciak-Piecka, J. Drabik, D. Jaque and L. Marciniak, *Phys. Chem. Chem. Phys.*, 2020, **22**, 25949–25962.
- 12 D. A. Gállico and M. Murugesu, *ACS Appl. Mater. Interfaces*, 2021, **13**, 47052–47060.
- 13 W. M. Yen, S. Shionoya and H. Yamamoto, *Phosphor handbook*, CRC Press, 2nd edn, 2007, pp. 844–885.
- 14 C. Piguet, J. C. G. Bünzli, G. Bernardinelli, G. Hopfgartner, A. F. Williams, J. C. G. Bünzli, G. Bernardinelli and G. Hopfgartner, *J. Am. Chem. Soc.*, 1993, **115**, 8197–8206.
- 15 D. Zhao, D. Yue, L. Zhang, K. Jiang and G. Qian, *Inorg. Chem.*, 2018, **57**, 12596–12602.